This is the peer-reviewed, final accepted version for American Mineralogist, published by the Mineralogical Society of America.
The published version is subject to change. Cite as Authors (Year) Title. American Mineralogist, in press.
DOI: https://doi.org/10.2138/am-2021-7621. http://www.minsocam.org/

7621 Revision 3

Discovery of terrestrial allabogdanite $(Fe,Ni)_2P$, and the effect of Ni and Mo substitution on the barringerite-allabogdanite high-pressure transition

Sergey N. Britvin[1,2*], Oleg S. Vereshchagin[1], Vladimir V. Shilovskikh[1,3], Maria G. Krzhizhanovskaya[1], Liudmila A. Gorelova[1], Natalia S. Vlasenko[1], Anna S. Pakhomova[4], Anatoly N. Zaitsev[1], Andrey A. Zolotarev[1], Maxim Bykov[5], Maksim S. Lozhkin[1], and Fabrizio Nestola[6]

[1]Saint-Petersburg State University, Universitetskaya Nab. 7/9, 199034 St. Petersburg, Russia
[2]Kola Science Center of Russian Academy of Sciences, Fersman Str. 14, 184209 Apatity, Murmansk Region, Russia
[3]Institute of Mineralogy, Urals Branch of Russian Academy of Science, 456317 Miass, Russia
[4]Deutsches Elektronen-Synchrotron (DESY), D-22607 Hamburg, Germany
[5]Geophysical Laboratory, Carnegie Institution of Washington, Washington, DC 20015, U.S.A.
[6]Dipartimento di Geoscienze, Università degli Studi di Padova, Via G. Gradenigo 6, I-35131 Padova, Italy

Always consult and cite the final, published document. See http:/www.minsocam.org or GeoscienceWorld

This is the peer-reviewed, final accepted version for American Mineralogist, published by the Mineralogical Society of America.
The published version is subject to change. Cite as Authors (Year) Title. American Mineralogist, in press.
DOI: https://doi.org/10.2138/am-2021-7621. http://www.minsocam.org/

Abstract

Minerals formed at high pressures are sensitive indicators of extreme pressure-temperature conditions that occur in nature. The discovery of the high-pressure polymorph of $(Fe,Ni)_2P$, allabogdanite in the surficial pyrometamorphic rocks of the Hatrurim Formation (the Mottled Zone) surrounding the Dead Sea basin in Israel is the first terrestrial occurrence of a mineral previously only found in iron meteorites. Stepwise annealing experiments demonstrate that allabogdanite is metastable at ambient pressure and that it irreversibly transforms into its low-pressure polymorph, barringerite, upon heating to 850±50°C. High-pressure high-temperature diamond-anvil cell (DAC) experiments confirm the results of annealing experiments. The DAC data indicate that Hatrurim allabogdanite is metastable below 7.4 GPa, and the low- to high-pressure phase transition (barringerite→allabogdanite) occurs at 25±3 GPa and 1400±100°C. The observed transition pressure of Hatrurim allabogdanite is significantly higher than that of pure synthetic Fe_2P (8 GPa), due to partial substitution of Fe for Ni (4 wt.%) and Mo (2.5 wt.%). Because the influence of substituting impurities on the conditions of phase transitions can be unexpectedly strong, our findings confirm that caution should be exercised when extrapolating data from experiments on synthetic compounds to natural systems. Based on the discovery of terrestrial allabogdanite $(Fe,Ni)_2P$ coupled with experiments probing the phase transitions in this natural composition, we contend that terrestrial allabogdanite formed via transformation from barringerite and posit potential scenarios of its formation.

Keywords: allabogdanite, barringerite, phosphide, Fe_2P, high pressure, crystal structure, phase transitions, Fe−Ni−P system

Always consult and cite the final, published document. See http:/www.minsocam.org or GeoscienceWorld

This is the peer-reviewed, final accepted version for American Mineralogist, published by the Mineralogical Society of America.
The published version is subject to change. Cite as Authors (Year) Title. American Mineralogist, in press.
DOI: https://doi.org/10.2138/am-2021-7621. http://www.minsocam.org/

Introduction

The area of the Eastern Mediterranean in the historical region of the Southern Levant bears the remnants of an enigmatic rock complex known as the Mottled Zone or the Hatrurim Formation (Figure 1) (Gross 1977; Vapnik et al. 2007). This formation represents the world's largest field of sedimentary rocks subjected to combustion metamorphism (pyrometamorphism) – the processes of surficial high-temperature calcination and fusion of sediments that produces mineral assemblages resembling cement clinkers or basic igneous rocks (Sokol et al. 2019). Numerous outcrops of the Mottled Zone span an area of 150×200 km^2 on both sides of the Dead Sea, encompassing the Judean and Negev deserts in Israel, Palestinian Authority and Transjordan Plateau in West-Central Jordan, with several patches mapped as far north as the Sea of Galilee (Kinneret) (the Maqarin site) (Figure 1). These exposed outcrops are likely remnants of wider fields deflated by later erosion (Matmon 2017). The largest preserved Mottled Zone massifs are the Daba-Siwaqa complex in West-Central Jordan (>300 km^2) and the Hatrurim Basin in Israel (~50 km^2) (Figure 1). Geological dating of the Mottled Zone has produced a range of ages, with the majority falling between 16 and 2.5 Ma (million years) (see a review in Sokol et al. 2019).

The mineralogy of the Mottle Zone rock suite is diverse and contains both highly reduced (e.g., Britvn et al. 2015; Galuskna et al. 2017) and highly oxidized mineral assemblages (Sokol et al. 2011; Juroszek et al. 2020), including those more characteristic of meteorites than terrestrial rocks (Weber and Bischoff 1994; Galuskina et al. 2016). Phosphides are typical accessory minerals in the Mottled Zone and have been identified in several localities at both sides of the Dead Sea, in Israel and West-Central Jordan. (Britvin et al. 2015, 2019a,c, 2020a,b,c). Phosphides typically form under highly reducing conditions and contain phosphorus in an oxidation state lower than zero. These minerals are commonly encountered in iron meteorites, whereas phosphorous normally occurs in its oxidized form in minerals from the Earth's crust. Since phosphides are considered the most likely source of low-

Always consult and cite the final, published document. See http:/www.minsocam.org or GeoscienceWorld

78 valent phosphorus in the prebiotic history of our planet (Bryant and Kee 2006; Gull et al. 2015; Pasek
79 2017), their discovery in the Mottled Zone has prompted the hypothesis of a terrestrial source of
80 prebiotic phosphorus on early Earth (Britvin et al. 2015). The superficial combustion of sediments that
81 give rise to the Mottled Zone mineral assemblage occurred at high-temperatures (from 800 to 1400°C)
82 but low-pressures (near-atmospheric); hence all hypotheses aimed at explaining the origin of this rock
83 suite follow a "low-pressure" paradigm (Gross 1977; Vapnik et al. 2007; Sokol et al. 2019). The recent
84 discovery of allabogdanite, $(Fe,Ni)_2P$, a high pressure polymorph of barringerite in the Mottled Zone,
85 which is described in this paper, calls into question this prevailing low-pressure paradigm. However,
86 because allabogdanite may contain substantial amounts of Ni and Mo substituting for Fe, a direct
87 comparison of its formation conditions with those determined for synthetic high-pressure Fe_2P is
88 problematic. Therefore, we performed high-pressure experiments aimed at determining the stability
89 field of the Dead Sea allabogdanite to inform the discussion of what geological processes may have
90 produced the allabogdanite-bearing assemblages of the Mottled Zone.

91 Allabogdanite (orthorhombic, structure type Co_2Si) and barringerite (hexagonal, structure type
92 Fe_2P) are polymorphs of Fe_2P. The relationship between their unit cells is sketched in Figure 2. Both
93 minerals commonly contain Ni substituting for Fe (Britvin et al. 2019b, 2020c). Barringerite was
94 discovered in the Ollague pallasite (Buseck 1969). This mineral, with substantial Ni, was subsequently
95 reported from several meteoritic and terrestrial occurrences (a brief review is given in Britvin et al.
96 2020c). In all cases, the mineral with composition $(Fe,Ni)_2P$ was described as barringerite, as no other
97 polymorphs of $(Fe,Ni)_2P$ were known. Recently, a complete solid solution between barringerite and
98 transjordanite (natural hexagonal Ni_2P) was shown (Britvin et al. 2020c). Allabogdanite was discovered
99 in the Onello meteorite (iron anomalous, Ni-rich ataxite) (Britvin et al. 2002). The high-pressure origin
100 of the mineral was not suggested at that time, because no experimental data on phase transitions of
101 $(Fe,Ni)_2P$ existed. Subsequently, Dera et al. (2008) showed that orthorhombic Fe_2P (i.e., having

Always consult and cite the final, published document. See http:/www.minsocam.org or GeoscienceWorld

allabogdanite structure) is a high-pressure phase metastable below 8 GPa. Recently, allabogdanite was found in two more Ni-rich ataxites (Santa Catharina and Barbianello) (Britvin et al. 2019b). Allabogdanite from meteorites is enriched in Ni (up to 0.8 Ni atoms per formula unit). However, the stability field of Fe_2P–Ni_2P solid solutions with this structure is not known. Pure Ni_2P does not transform to allabogdanite-type polymorph even at 50 GPa (Dera et al. 2009). Allabogdanite was not encountered on Earth prior to the present work.

Materials and Methods

Scanning electron microscopy (SEM) and electron microprobe analysis (EMPA). Chemical homogeneity of phosphides was inspected in the polished rock sections with an Hitachi S-3400N SEM equipped with an Oxford Instruments AzTec Energy X-Max 20 EDX detector. EMPA data were acquired with an INCA WAVE 500 WDX spectrometer using the following standards: GaP (P), metallic Cr, V, Fe, Co and Ni (all *K*α lines), Mo (Mo*L*α), at 20 kV and 15 nA. ***Electron backscatter diffraction (EBSD).*** Polished sections intended for EBSD study were subjected to reactive ion etching (RIE) with Ar^+ ions using an Oxford Instruments IonFab-300 instrument (500 V, 2.4 mA cm^{-2} flow current), etching time was 20 min. EBSD analyses were carried out by means of an Oxford Instruments Nordlys-HKL EBSD detector operated at 30 kV and 1.5 nA in focused beam mode with a 70° tilted stage. The samples were coated with a ~2 nm carbon film and grounded with carbon tape. Identification of allabogdanite and barringerite was performed by matching their EBSD patterns with the reference structures (ICSD 94577 and 70115). The details of EBSD procedures are given in Table S1. ***Single-crystal X-ray diffraction (SCXRD) and crystal structure.*** Allabogdanite grain #1 (Figure 3) and barringerite grain #5, as well as two-phase grain #3 were extracted for crystal structure measurements. SCXRD datasets were collected by means of a Bruker Kappa APEX DUO CCD diffractometer (Mo*K*α, 50 kV, 0.6 mA) and processed using standard SCXRD routines incorporated

Always consult and cite the final, published document. See http:/www.minsocam.org or GeoscienceWorld

into the Bruker APEX2 software. Crystal structures were solved and refined using the *SHELX*-2018 set of programs (Sheldrick 2015) incorporated into the Olex2 graphical user shell (Dolomanov et al. 2009). The details of SCXRD study can be retrieved from CIF files in Supplementary Data. ***Annealing experiments, powder X-ray diffraction (PXRD) and post-annealing X-ray single-crystal diffraction (SCXRD).*** Allabogdanite grains #7 and #13 (Figure 3) were subjected to stepwise heating in a Netzsch STA 449 F1 differential scanning calorimeter at a ramp rate of 10° min^{-1}, using 4-mm Pt pan at 50 mL min^{-1} Ar flow (99.9994 % Ar). In order to avoid possible reaction between allabogdanite and Pt upon heating, mineral grains were placed onto 1-mm thick diamond plate used as an interface between allabogdanite and Pt pan. The structural state of stepwise-heated grains was inspected using non-destructive PXRD including the following set-up: Rigaku RAXIS Rapid II diffractometer (semi-cylindrical image plate, r=127.4 mm, Co $K\alpha$, rotating anode, 40 kV, 15 mA, microfocus X-ray optics). PXRD image acquisitions were conducted in Debye-Scherrer geometry using a Gandolfi method, with an exposure time 60 min. The obtained images were transformed into the profile data using osc2xrd program (Britvin et al. 2017a) and fitted with a Pawley method implemented into a Bruker Topas 4.2 software. The first heating run of grain #7 was interrupted at 600°C, followed by cooling the grain to room temperature, picking up the annealed grain and inspecting its structural state. Subsequent heating/PXRD runs were performed stepwise with 50° step. The allabogdanite→barringerite transition of grain #7 was detected between 800 and 850°C (Figure 7). The same transition of the grain #13 was detected between 750 and 800°C. Therefore, average transition temperature was found to be 800±50°C. The grain #13 (originally composed solely of allabogdanite) was studied by means of SCXRD *after* thermally induced transition to barringerite. The SCXRD procedures were the same as described above. The rotation matrices of barringerite formed after thermally induced allabogdanite→barringerite transition are given in Table 4. ***In situ X-ray single-crystal high-pressure-high-temperature experiments***. The experiments in laser-heated diamond anvil cells (LHDAC) were carried out at the

Always consult and cite the final, published document. See http:/www.minsocam.org or GeoscienceWorld

This is the peer-reviewed, final accepted version for American Mineralogist, published by the Mineralogical Society of America.
The published version is subject to change. Cite as Authors (Year) Title. American Mineralogist, in press.
DOI: https://doi.org/10.2138/am-2021-7621. http://www.minsocam.org/

P02.2 Extreme Conditions Beamline (ECB) of PETRA III storage ring of Deutsches Elektronen Synchrotron (DESY) light source (Hamburg, Germany). The layout of a beamline involves a 1-circle (ω-rotation) goniometer equipped with a stage holder designed for X-ray studies in diamond-anvil cells (DAC). Symmetric Mao-type DACs with culet diameters of 400 and 150 μm were used for pressure generation in the experiments #1 and #2, respectively. The sample chambers with approximate diameters of 200 and 80 μm were obtained by drilling the preintended rhenium gaskets. ~5 μm ruby balls were placed in each sample chamber for initial pressure estimation (using luminescence spectrum), whereas 10-15 μm chips of Au foil were used for pressure determination during the experiments. 20-30 μm single-crystal fragments of Mo- and Ni-enriched allabogdanite have been placed in each DAC along with the pressure standards. The DACs were loaded with neon as a pressure-transmitting medium using an in-house gas loading system at PETRA III. The monochromatic X-ray beam had a cross-section of 2×2 μm^2 and a wavelength of 0.2892 Å. The Perkin Elmer XRD 1621 detector (CsI bonded amorphous silicon, 2048×2048 pixels, 200μm square pixel size) was placed ~404 mm away from the DAC. The detector was calibrated with a CeO_2 powder standard using the DIOPTAS program (Prescher and Prakapenka 2015). Prior to the high-pressure-high-temperature experiments, the unit-cell parameters of allabogdanite were determined at ambient conditions using the single-crystal X-ray datasets collected from –32 to 32° (ω) at the frame sweep of 0.5°. Data processing and integration routines were carried out by means of a Rigaku Oxford Diffraction CrysAlis Pro package, using orthoenstatite as an external calibration standard. The 200W on-axis Yb-fiber laser (1064 nm) allowed double-sided heating of a ~15×15 μm^2 area of the allabogdanite single crystals between 1300-1600°C. The temperature was determined with a precision ±100°C using a black-body excitation spectrum. Each series of single-crystal X-ray experiments included stepwise compression of the crystal in DAC, followed by a double-sided laser heating for 5-8 minutes. During the heating, the laser beam was gradually moved across the crystal, in order to achieve as uniform heating as possible.

Always consult and cite the final, published document. See http:/www.minsocam.org or GeoscienceWorld

After cooling the crystal for ~2 min, the single-crystal X-ray datasets were collected at each pressure step. In the experiment #1, the initial pressure was set at 2.0 GPa. The crystal was then compressed to 4.8 GPa followed by the first laser heating to 1350°C. The complete allabogdanite→barringerite transition was observed after 5 min of heating time. The two additional compression-heating runs were conducted up to 19.6 GPa at 1350°C, without reaching the expected low- to high-pressure phase transition point. The experiment #2 was started at 7.4 GPa. The allabogdanite→barringerite phase transition was completed within 8 min of laser heating to 1350°C. After several compression/heating steps, the barringerite→allabogdanite conversion was accomplished at 28.4 GPa and 1400°C for 8 min. Further compression/heating runs to 39 GPa and 1400°C did not reveal any phase transitions.

Results

Occurrence of terrestrial allabogdanite

Allabogdanite was identified in several rock samples collected in the midstream of the Halamish Wadi (Nahal Halamish) in the Hatrurim Basin, Israel, near the southern sub-basin of the Dead Sea (Figure 1b). Phosphide assemblages of the Halamish Wadi were the first discovered in the Mottled Zone (Britvin et al. 2015, 2017b, 2020c and the references cited therein). Allabogdanite is associated with barringerite; both minerals typically occur as rounded nodules up to 0.5 mm in diameter, disseminated in a matrix dominated by a micro-brecciated diopside (up to 70%) (Figure 3). Chemical composition of the latter corresponds to pure $CaMgSi_2O_6$ as the contents of other elements lie below detection limit of our WDX detector (~0.05 wt.%) and single-crystal X-ray diffraction confirmed the diopside structure. No other anhydrous silicates were detected. However, the microbreccia is cemented by a range of poorly crystallized, late hydrothermal (or possibly secondary) hydrous silicates of Ca, Mg, Fe and sometimes Ni, as well as calcite and aragonite. Small grains of hematite, magnetite and pyrrhotite are sporadically encountered. A notable chemical feature of these microbreccias is the almost complete lack of Al-containing minerals.

Always consult and cite the final, published document. See http:/www.minsocam.org or GeoscienceWorld

This is the peer-reviewed, final accepted version for American Mineralogist, published by the Mineralogical Society of America.
The published version is subject to change. Cite as Authors (Year) Title. American Mineralogist, in press.
DOI: https://doi.org/10.2138/am-2021-7621. http://www.minsocam.org/

198 Allabogdanite is steel-gray colour with metallic lustre; the crushed surfaces are metallic-white.
199 The mineral is brittle and lacks recognizable cleavage; the Moh's hardness is between 5 and 6. In the
200 polished sections under reflected light, allabogdanite is yellowish-white with no observable
201 birefringence and very week anisotropy. These properties are similar to those of meteoritic
202 allabogdanite (Britvin et al. 2002) and make allabogdanite optically indistinguishable from barringerite
203 (Figure 3, 4). The peripheral parts of allabogdanite (and barringerite) grains are commonly corroded
204 and replaced by the rims of murashkoite, FeP (Britvin et al. 2019c) (Figure 4).
205
206 **Chemical composition and structural study**
207 A phosphide-rich section of one of the diopside microbreccias was chosen for further examination.
208 Each phosphide grain was subjected to electron microprobe analysis (Table 1) and crystallographic
209 investigation (Table 2). With the exception of grain #9, allabogdanite and barringerite are close to
210 endmember compositions with 1.6 +/− 0.2 and 1.8 +/− 0.2 wt% Ni, respectively, while Co and Mo are
211 below 0.5 wt%. We conducted structure analysis with single-crystal diffraction for allabogdanite and
212 barringerite crystals of nearly endmember compositions (Table 2). The detailed results of structure
213 refinements can be retrieved from crystallographic information file (CIF) in the Supplementary Data.
214 Electron backscatter diffraction (EBSD) reveals no orientational relationship between
215 allabogdanite and barringerite (Figs. 3, 4). Barringerite occurs as single-crystal grains, many of which
216 are in part, or completely, replaced by allabogdanite (Figure 4). The latter forms fine multiple
217 interpenetration twins (trillings) formed by the rotation of twin domains about the *b*-axis, as revealed
218 by EBSD orientation mapping (Figure 3, 4). The compositions of allabogdanite and barringerite sectors
219 of those grains are identical (Table 1) and they can be distinguished only by their crystal structure. In
220 order to unambiguously confirm the presence of allabogdanite trillings, a two-phase grain #3 (Figure 4)
221 was extracted from the polished section for single-crystal structural examination. The latter confirmed

Always consult and cite the final, published document. See http:/www.minsocam.org or GeoscienceWorld

(Table 3) the existence of a three-component interpenetrating twin (trilling) of allabogdanite (Figure 4b). It is important with regard to further implications that allabogdanite trillings do not have any regular crystallographic relations to barringerite – the polymorphs are intergrown in a random way (Figure 4c). An extreme example of multiple intergrowth and twinning of allabogdanite is shown in Figure 5. It can be seen that the twin boundaries of allabogdanite domains do not coincide with, but instead penetrate or abut the habit and interphase boundaries of phosphide grains. The occurrence of twinning distinguishes terrestrial allabogdanite from the mineral of meteoritic origin (Britvin et al. 2019b) which always appear as single crystals (Figure 6).

Metastable state of terrestrial allabogdanite

The metastable state of allabogdanite was confirmed from stepwise annealing experiments aimed at determining the allabogdanite→barringerite transition temperature. The experiment conditions are reported in the Supplementary Data. It was found that: (1) allabogdanite→barringerite transition occurs at 800±50°C (Figure 7), (2) this transition is irreversible at atmospheric pressure, (3) barringerite formed by thermally induced transition forms multi-crystal grains rather than single crystals and, (4) orientation relationships between twin domains of primary allabogdanite are not inherited by the newly formed barringerite (Table 4). Therefore, one can suggest that allabogdanite→barringerite conversion proceeds via reconstructive, rather than displacive phase transformation, similar to the process previously reported for synthetic Fe_2P (Dera et al. 2008). The physical integrity of mixed allabogdanite-barringerite grains is maintained due to the small difference (0.8 - 2.5%) in molar volume (and thus density) between allabogdanite and barringerite (Table 2 and 5), mitigating residual strains in the crystals. The 1-bar transition temperature presented here is consistent with the earlier data reported by Senateur et al. (1976) for synthetic Fe_2P, but 200°C lower than that reported by Dera et al. (2008).

Always consult and cite the final, published document. See http:/www.minsocam.org or GeoscienceWorld

This is the peer-reviewed, final accepted version for American Mineralogist, published by the Mineralogical Society of America.
The published version is subject to change. Cite as Authors (Year) Title. American Mineralogist, in press.
DOI: https://doi.org/10.2138/am-2021-7621. http://www.minsocam.org/

In situ high-pressure high-temperature experiments

In order to determine the phase transition conditions for the terrestrial allabogdanite, a fragment of the most Ni- and Mo-rich grain was chosen (denoted by "X" in Figure 5a and Table 1), as it was expected that the incorporation of Ni and Mo may substantially affect the pressure-temperature phase boundary. This grain was crushed and studied by *in situ* high-pressure high-temperature single-crystal X-ray diffraction in diamond anvil cells (DAC). The details of the experiments are provided in the Supplementary Data. The results are summarized in Table 5 and graphically expressed in Figure 8. Based on initial heating runs performed at 4.8 and 7.4 GPa and 1350±100°C, it was found that allabogdanite irreversibly transforms into barringerite within ~5-8 min at both pressures. This means that in order to be preserved (though metastable) at ambient or low-pressure conditions, allabogdanite has to be quenched below transition temperature at pressures exceeding 7.4 GPa.

Additionally, a series of high-temperature compression experiments were performed on the fragments of the same Ni- and Mo-rich grain ("X" in Figure 5a), to determine the onset of barringerite→allabogdanite transition. It is noteworthy that, in contrast to the conditions of single-crystal experiment reported by Dera et al. (2008), each compression step in our experiments was accompanied by laser heating. Based on our experiments at 1400±100°C, the barringerite → allabogdanite transition of the Ni- and Mo-bearing grain occurs at the unexpectedly high pressure of 25±3 GPa (Table 5, Figure 8). The measured transition pressure of this grain is significantly greater than the 8 GPa obtained for pure synthetic Fe_2P (Senateur et al. 1976; Dera et al. 2008). Another important result of these experiments is that in contrast to the observations of synthetic Fe_2P (Dera et al. 2008), Hatrurim Formation allabogdanite has a higher density at the transition point than barringerite. The observed change in density (D) is small (0.8%) and thus fits the $\Delta D/D$ trend typical of polymorph pairs (Tschauner 2019).

Always consult and cite the final, published document. See http:/www.minsocam.org or GeoscienceWorld

This is the peer-reviewed, final accepted version for American Mineralogist, published by the Mineralogical Society of America.
The published version is subject to change. Cite as Authors (Year) Title. American Mineralogist, in press.
DOI: https://doi.org/10.2138/am-2021-7621. http://www.minsocam.org/

Implications

Though allabogdanite was discovered 18 years ago (Britvin et al. 2002), it wasn't until 2008 that it was shown to be a high-pressure phase (Dera et al. 2008), as the high-pressure relationships in the Fe–Ni–P system have attracted less attention compared to the silicate and oxide systems (Tomioka and Miyahara 2017; Tschauner 2019). The Fe–Ni–P ternary is one of the most important reduced systems in the Solar System, as phosphides were condensed during the early stages of the nebula formation (Pasek 2019) and are argued to be substantial constituents of planetary interiors (Scott et al. 2007, 2008; Gu et al. 2011, 2014; He et al. 2019). This work is the first to report terrestrial allabogdanite and the first high-pressure study of natural allabogdanite. Previous work on synthetic Fe_2P found that 8 GPa is the low-pressure limit of phase transformation (Senateur et al. 1973; Dera et al. 2008; Minin et al. 2019). The unexpectedly high transition pressure of 25±3 GPa for natural allabogdanite can be explained by the doping effects of Ni (4 wt.%) and Mo (2.5 wt.%), consistent with previous studies that have shown that synthetic Ni_2P is stable in the barringerite-type structure up to at least 50 GPa (Dera et al. 2009). The influence of Mo substitution on the phase transition is less well understood, because both synthetic and natural MoNiP (monipite) adopt the barringerite structure at ambient conditions (Guérin and Sergent 1977a; Ma et al. 2014), whereas synthetic FeMoP crystallizes in the orthorhombic (allabogdanite-type) system (Guérin and Sergent 1977b). The difference in the phase boundaries in synthetic versus natural terrestrial allabogdanite shown in this study underline the importance of exercising caution whilst using data on endmembers to extrapolate to more compositionally complex natural systems as the influence of substituting impurities on the conditions of phase transitions can be significant.

The experimentally reconstructed formation conditions of allabogdanite from the Mottled Zone imply that the terrestrial allabogdanite formed from the low-pressure barringerite precursor must have been subjected to pressures of at least 25±3 GPa. However, there is a major obstacle in adopting this high-pressure formation scenario, which is the association of terrestrial allabogdanite with pure

Always consult and cite the final, published document. See http:/www.minsocam.org or GeoscienceWorld

diopside. Previous studies indicate that diopside is stable under compression up to 17 GPa at 1000-1400°C but decomposes into a mixture of silicate phases at higher pressures (Kim et al. 1994; Oguri et al. 1997; Akaogi et al. 2004). Taking into account the accuracy of our pressure measurements (±3 GPa), there is a gap of at least 5 GPa between the upper stability limit of diopside and the recorded barringerite→allabogdanite transition point. This discrepancy makes it unlikely that allabogdanite formed as a result of an *in-situ* high-pressure shock event, e.g., a hypothetical Earth-meteoroid hypervelocity collision (French and Koeberl 2010) or any natural process mimicking high-pressure gas explosions (e.g., Wilk and Kenkmann 2016). Furthermore, there is no geological evidence for a large impact structure in the well-studied Dead Sea area (e.g., Garfunkel and Ben-Avraham 1996), including an absence of other high pressure minerals. The mineral composition and texture of the allabogdanite-bearing diopside microbreccia (Figure 2) resembles mantle diopsidites from ophiolite complexes (Python et al. 2007; Ishimaru and Arai 2011; Akizawa and Arai 2014). However, there are no documented mantle lithologies across a well-explored area surrounding the Dead Sea Transform (e.g., Ten Brink et al. 1999). Therefore, the origin of terrestrial allabogdanite in the rocks of the Mottled Zone remains unresolved and adds to the number of mineralogical enigmas of this unusual metamorphic complex.

Acknowledgements We thank Mikhail Murashko and Yevgeny Vapnik for loaning the specimens used in this study. The authors are thankful to Associate Editors Oliver Tschauner and Elizabeth Thompson, reviewers Laurence Garvie, Robert Hazen and an anonymous reviewer for their helpful comments, discussions and invaluable linguistic help which considerably enhanced the quality of the manuscript. This research was financially supported by Russian Science Foundation, grant 18-17-00079. High-pressure studies were carried out at the light source PETRA III at DESY, a member of the Helmholtz Association (HGF), proposal I-20190536. The authors acknowledge the Resource Center of X-ray

Always consult and cite the final, published document. See http:/www.minsocam.org or GeoscienceWorld

This is the peer-reviewed, final accepted version for American Mineralogist, published by the Mineralogical Society of America.
The published version is subject to change. Cite as Authors (Year) Title. American Mineralogist, in press.
DOI: https://doi.org/10.2138/am-2021-7621. http://www.minsocam.org/

diffraction studies, "Geomodel" Resource Centre, Nanophotonics and Nanotechnology Resource Centers of Saint-Petersburg State University for providing instrumental and computational resources.

References cited

Akaogi, M., Yano, M., Tejima, Y., Iijima, M., and Kojitani, H. (2004) High-pressure transitions of diopside and wollastonite: Phase equilibria and thermochemistry of $CaMgSi_2O_6$, $CaSiO_3$ and $CaSi_2O_5$-$CaTiSiO_5$ system. Physics of the Earth and Planetary Interiors, 143–144, 145–156.

Akizawa, N., and Arai, S. (2014) Petrology of mantle diopsidite from Wadi Fizh, northern Oman ophiolite: Cr and REE mobility by hydrothermal solution. Island Arc, 23, 312–323.

Britvin, S.N., Rudashevsky, N.S., Krivovichev, S.V., Burns, P.C., and Polekhovsky, Y.S. (2002) Allabogdanite, $(Fe,Ni)_2P$, a new mineral from the Onello meteorite: the occurrence and crystal structure. American Mineralogist, 87, 1245–1249.

Britvin, S.N, Murashko, M.N., Vapnik, Ye., Polekhovsky, Yu.S., and Krivovichev, S.V. (2015) Earth's phosphides in Levant and insights into the source of Archean prebiotc phosphorus. Scientific Reports, 5, 8355.

Britvin, S.N., Dolivo-Dobrovolsky, D.V., and Krzhizhanovskaya, M.G. (2017a) Software for processing the X-ray powder diffraction data obtained from the curved image plate detector of Rigaku RAXIS Rapid II diffractometer. Zapiski Rossiiskogo Mineralogicheskogo Obshchestva, 146, 104–107.

Britvin, S.N., Murashko, M.N., Vapnik, E., Polekhovsky, Yu. S., and Krivovichev, S.V. (2017b) Barringerite Fe_2P from pyrometamorphic rocks of the Hatrurim Formation, Israel. Geology of Ore Deposits, 59, 619–625.

Always consult and cite the final, published document. See http:/www.minsocam.org or GeoscienceWorld

This is the peer-reviewed, final accepted version for American Mineralogist, published by the Mineralogical Society of America.
The published version is subject to change. Cite as Authors (Year) Title. American Mineralogist, in press.
DOI: https://doi.org/10.2138/am-2021-7621. http://www.minsocam.org/

342 Britvin, S.N., Murashko, M.N., Vapnik, Ye., Polekhovsky, Yu.S., Krivovichev, S.V., Vereshchagin,
343 O.S., Vlasenko, N.S., Shilovskikh, V.V., and Zaitsev, A.N. (2019a) Zuktamrurite, FeP_2, a new
344 mineral, the phosphide analogue of löllingite, $FeAs_2$. Physics and Chemistry of Minerals, 46,
345 361–369.
346 Britvin, S.N., Shilovskikh, V.V., Pagano, R., Vlasenko, N.S., Zaitsev, A.N., Krzhizhanovskaya, M.G.,
347 Lozhkin, M.S., Zolotarev, A.A., and Gurzhiy, V.V. (2019b) Allabogdanite, the high-pressure
348 polymorph of $(Fe,Ni)_2P$, a stishovite-grade indicator of impact processes in the Fe–Ni–P system.
349 Scientific Reports, 9, 1047.
350 Britvin, S.N., Vapnik, Ye., Polekhovsky, Yu.S. and Krivovichev, S.V., Krzhizhanovkaya M.G.,
351 Gorelova, L.A., Vereshchagin, O.S., Shilovskikh, V.V., and Zaitsev, A.N. (2019c) Murashkoite,
352 FeP, a new terrestrial phosphide from pyrometamorphic rocks of the Hatrurim Formation,
353 Southern Levant. Mineralogy and Petrology, 113, 237–248.
354 Britvin, S.N., Murashko, M.N., Vapnik, Ye., Polekhovsky, Yu.S., Krivovichev, S.V., Vereshchagin,
355 O.S., Shilovskikh, V.V., Vlasenko, N.S., and Krzhizhanovskaya, M.G. (2020a) Halamishite,
356 Ni_5P_4, a new terrestrial phosphide in the Ni–P system. Physics and Chemistry of Minerals, 2020,
357 3.
358 Britvin, S.N., Murashko, M.N., Vapnik, Ye., Polekhovsky, Yu.S., Krivovichev, S.V., Vereshchagin,
359 O.S., Shilovskikh, V.V., and Krzhizhanovskaya, M.G. (2020b) Negevite, the pyrite-type NiP_2, a
360 new terrestrial phosphide. American Mineralogist, 105, 422–427.
361 Britvin, S.N., Murashko, M.N., Vapnik, Ye., Polekhovsky, Yu.S., Krivovichev, S.V.,
362 Krzhizhanovskaya, M.G., Vereshchagin, O.S., Shilovskikh, V.V., and Vlasenko, N.S. (2020c)
363 Transjordanite, Ni_2P, a new terrestrial and meteoritic phosphide, and natural solid solutions
364 barringerite–transjordanite (hexagonal Fe_2P–Ni_2P). American Mineralogist, 105, 428–436.

Always consult and cite the final, published document. See http:/www.minsocam.org or GeoscienceWorld

This is the peer-reviewed, final accepted version for American Mineralogist, published by the Mineralogical Society of America.
The published version is subject to change. Cite as Authors (Year) Title. American Mineralogist, in press.
DOI: https://doi.org/10.2138/am-2021-7621. http://www.minsocam.org/

Bryant, D.E., and Kee, T.P. (2006) Direct evidence for the availability of reactive, water soluble phosphorus on the early Earth. H-Phosphinic acid from the Nantan meteorite. Chemical Communications, 2006, 2344–2346.

Buseck, P.R. (1969) Phosphide from meteorites: Barringerite, a new iron-nickel mineral. Science, 165, 169–171.

Dera, P., Lavina, B., Borkowski, L.A., Prakapenka, V.B., Sutton, S.R., Rivers, M.L., Downs, R.T., Boctor, N.Z., and Prewitt, C.T. (2008) High-pressure polymorphism of Fe_2P and its implications for meteorites and Earth's core. Geophysical Research Letters, 35, L10301.

Dera, P., Lavina, B., Borkowski, L. A., Prakapenka, V. B., Sutton, S. R., Rivers, M. L., Downs, R. T., Boctor, N. Z., and Prewitt, C. T. (2009) Structure and behavior of the barringerite Ni end-member, Ni_2P, at deep Earth conditions and implications for natural Fe-Ni phosphides in planetary cores. Journal of Geophysical Research, 114, B03201.

Dolomanov, O.V., Bourhis, L.J., Gildea, R.J., Howard, J.A., and Puschmann, H. (2009) OLEX2: a complete structure solution, refinement and analysis program. Journal of Applied Crystallography, 42, 339–341.

French, B.M., and Koeberl, C. (2010) The convincing identification of terrestrial meteorite impact structures: what works, what doesn't, and why. Earth Science Reviews, 98, 123–170.

Galuskina, I.O., Galuskin, E.V., and Vapnik, Y.A. (2016) Terrestrial merrillite. 2nd European Mineralogy Conference, Plinius, 42, 563.

Galuskina, I.O., Galuskin, E.V., Prusik, K., Vapnik Y., Juroszek, R., Jeżak, L. and Murashko, M. (2017) Dzierżanowskite, $CaCu_2S_2$ – a new natural thiocuprate from Jabel Harmun, Judean Desert, Palestine Autonomy, Israel. Mineralogical Magazine, 81, 777–789.

Garfunkel, Z., and Ben-Avraham, Z. (1996) The structure of the Dead Sea basin. Tectonophysics, 266, 155–176.

Always consult and cite the final, published document. See http:/www.minsocam.org or GeoscienceWorld

389 Geller, Y.I., Burg, A., Halicz, L., and Kolodny, Y. (2012) System closure during the combustion
390 metamorphic "Mottled Zone" event, Israel. Chemical Geology, 334, 25–36.
391 Gross, S. (1977) The mineralogy of the Hatrurim formation, Israel. Geological Survey of Israel
392 Bulletin, 70, 1–80.
393 Gu, T., Wu, X., Qin, S., and Dubrovinsky, L. (2011) In situ high-pressure study of FeP: implications
394 for planetary cores. Physics of the Earth and Planetary Interiors, 184, 154–159.
395 Gu, T., Fei, Y., Wu, X., and Qin, S. (2014) High-pressure behavior of Fe_3P and the role of phosphorus
396 in planetary cores. Earth and Planetary Science Letters, 390, 296–303.
397 Guérin, R., and Sergent, M. (1977a) Structure crystalline de MoNiP. Acta Crystallographica, B33,
398 2820–2823.
399 Guérin, R., and Sergent., M. (1977b) Nouveaux arseniures et phosphures ternaires de molybdene ou de
400 tungstene et d'elements 3d, de formule: $M_{2-x}Me_xX$ (M = élément 3d; Me = Mo, W; X = As, P).
401 Materials Research Bulletin, 12, 381–388.
402 Gull, M., Mojica, M.A., Fernández, F.M., Gaul, D.A., Orlando, T.M., Liotta, C.L., and Pasek, M.A.
403 (2015) Nucleoside phosphorylation by the mineral schreibersite. Scientific Reports, 5, 17198.
404 He, X.-J., Guo, J.-Z., Wu, X., Huang, S.-X., Qin, F., Gu, X.-P., and Qin, S. (2019) Compressibility of
405 natural schreibersite up to 50 GPa. Physics and Chemistry of Minerals, 46, 91–99.
406 Ishimaru, S., and Arai, S. (2011) Peculiar Mg–Ca–Si metasomatism along a shear zone within the
407 mantle wedge: inference from fine-grained xenoliths from Avacha volcano, Kamchatka.
408 Contributions to Mineralogy and Petrology, 161, 703–720.
409 Juroszek, R., Krüger, B., Galuskina, I., Krüger, H., Vapnik, Ye., and Galuskin, E. (2020) Siwaqaite,
410 $Ca_6Al_2(CrO_4)_3(OH)_{12}\cdot 26H_2O$, a new mineral of the ettringite group from the pyrometamorphic
411 Daba-Siwaqa complex, Jordan. American Mineralogist 105, 409–421.

Always consult and cite the final, published document. See http:/www.minsocam.org or GeoscienceWorld

This is the peer-reviewed, final accepted version for American Mineralogist, published by the Mineralogical Society of America.
The published version is subject to change. Cite as Authors (Year) Title. American Mineralogist, in press.
DOI: https://doi.org/10.2138/am-2021-7621. http://www.minsocam.org/

412 Kim, Y.-H., Ming, L.C., and Manghnani, M.H. (1994) High-pressure phase transformations in a natural
413 crystalline diopside and a synthetic $CaMgSi_2O_6$ glass. Physics of the Earth and Planetary
414 Interiors, 83(1), 67–79.
415 Ma, C., Beckett, J.R., and Rossman, G.R. (2014) Monipite, MoNiP, a new phosphide mineral in a Ca-
416 Al-rich inclusion from the Allende meteorite. American Mineralogist, 99, 198–205.
417 Matmon, A. (2017) Landscape evolution along the Dead Sea Fault and its margins. In Ye. Enzel and O.
418 Bar-Yosef, Ed., Quaternary of the Levant, p. 391–400. Cambridge University Press, U.K.
419 Minin, D.A., Shatskiy, A.F., Litasov, K.D., and Ohfuji, H. (2019) The Fe–Fe_2P phase diagram at 6
420 GPa. High Pressure Research, 39, 50–68.
421 Novikov, I., Vapnik, Ye., and Safonova, I. (2013) Mud volcano origin of the Mottled Zone, South
422 Levant. Geoscience Frontiers, 4, 597–619.
423 Oguri, K., Funamori, N., Sakai, F., Kondo, T., Uchida, T., and Yagi, T. (1997) High-pressure and high-
424 temperature phase relations in diopside $CaMgSi_2O_6$. Physics of the Earth and Planetary Interiors,
425 104(4), 363–370.
426 Pasek, M.A. (2017) Schreibersite on the early Earth: scenarios for prebiotic phosphorylation.
427 Geoscience Frontiers, 8, 329–335.
428 Pasek, M.A. (2019) Phosphorus volatility in the early Solar nebula. Icarus, 317, 59–65.
429 Prescher, C., and Prakapenka, V.B. (2015) DIOPTAS: a program for reduction of two-dimensional X-
430 ray diffraction data and data exploration. High Pressure Research, 35, 223–230.
431 Python, M., Ceuleneer, G., Ishida, Y., Barrat, J.-A., and Arai, S. (2007) Oman diopsidites: a new
432 lithology diagnostic of very high temperature hydrothermal circulation in mantle peridotite below
433 oceanic spreading centres. Earth Planetary Science Letters, 255, 289–305.
434 Rigaku Oxford Diffraction. CrysAlisPro Software System Version 171.40.67a (Rigaku Corporation,
435 Oxford, UK, 2018).

Always consult and cite the final, published document. See http:/www.minsocam.org or GeoscienceWorld

This is the peer-reviewed, final accepted version for American Mineralogist, published by the Mineralogical Society of America.
The published version is subject to change. Cite as Authors (Year) Title. American Mineralogist, in press.
DOI: https://doi.org/10.2138/am-2021-7621. http://www.minsocam.org/

436 Scott, H.P., Huggins, S., Frank, M.R., Maglio, S.J., Martin, C.D., Meng, Y., Santillán, J., and Williams,
437 Q. (2007) Equation of state and high-pressure stability of Fe_3P-schreibersite: implications for
438 phosphorus storage in planetary cores. Geophysical Research Letters, 34, L06302.
439 Scott, H.P., Kiefer, B., Martin, C.D., Boateng, N., Frank, M.R., and Meng, Y. (2008) *P-V* equation of
440 state for Fe_2P and pressure-induced phase transition in Fe_3P. High Pressure Research, 28, 375–
441 384.
442 Senateur, J.P., Rouault, A., and Fruchart, R. (1976) Etude par spectrometrie Mossbauer des
443 transformations cristallographiques sous hautes pressions de MnFeAs et Fe_2P. Materials Research
444 Bulletin, 11, 631–636.
445 Sheldrick, G.M. (2015) A short history of SHELX. Acta Crystallographica A71, 3–8.
446 Sokol, E.V., Gaskova, O.L., Kokh, S.N., Kozmenko, O.A., Seryotkin, Yu.V., Vapnik, Ye., and
447 Murashko, M.N. (2011) Chromatite and its Cr^{3+}- and Cr^{6+}-bearing precursor minerals from the
448 Nabi Musa Mottled Zone complex, Judean Desert. American Mineralogist, 96, 659–674.
449 Sokol, E.V., Kokh, S.N., Sharygin, V.V., Danilovsky, V.A., Seryotkin, Yu.V., Liferovich, R.,
450 Deviatiiarova, A.S., Nigmatulina, E.N., and Karmanov, N.S. (2019) Mineralogical diversity of
451 Ca_2SiO_4-bearing combustion metamorphic rocks in the Hatrurim Basin: implications for storage
452 and partitioning of elements in oil shale clinkering. Minerals, 9, 465.
453 Ten Brink, U.S., Rybakov, M., Al-Zoubi, A.S., Hassouneh, M., Frieslander, U., Batayneh, A.T.,
454 Goldschmidt, V., Daoud, M.N., Rotstein, Y., and Hall, J.K. (1999). Anatomy of the Dead Sea
455 Transform; does it reflect continuous changes in plate motion? Geology, 27, 887–890.
456 Tomioka, N., and Miyahara, M. (2017) High-pressure minerals in shocked meteorites. Meteoritics and
457 Planetary Science, 52, 2017–2039.
458 Tschauner, O. (2019) High-pressure minerals. American Mineralogist, 104, 1701–1731.

Always consult and cite the final, published document. See http:/www.minsocam.org or GeoscienceWorld

This is the peer-reviewed, final accepted version for American Mineralogist, published by the Mineralogical Society of America.
The published version is subject to change. Cite as Authors (Year) Title. American Mineralogist, in press.
DOI: https://doi.org/10.2138/am-2021-7621. http://www.minsocam.org/

Vapnik, Ye., Sharygin, V.V., Sokol, E.V., and Shagam, R. (2007) Paralavas in a combustion metamorphic complex: Hatrurim Basin, Israel. Reviews in Engineering Geology, 18, 1–21.

Weber, D., and Bischoff, A. (1994) Grossite ($CaAl_4O_7$) – a rare phase in terrestrial rocks and meteorites. European Journal of Mineralogy, 6, 591–594.

Wilk, J., and Kenkmann, T. (2016). Formation of shatter cones in MEMIN impact experiments. Meteoritics & Planetary Science, 51, 1477–1496.

Always consult and cite the final, published document. See http:/www.minsocam.org or GeoscienceWorld

This is the peer-reviewed, final accepted version for American Mineralogist, published by the Mineralogical Society of America.
The published version is subject to change. Cite as Authors (Year) Title. American Mineralogist, in press.
DOI: https://doi.org/10.2138/am-2021-7621. http://www.minsocam.org/

Captions to the Figures

Figure 1. The Mottled Zone (Hatrurim Formation). (**a**) Distribution of the Mottled Zone outcrops (brown patches) in the Southern Levant. The largest areas are the Hatrurim Basin (Israel) and Daba-Siwaqa complex (Jordan). (**b**) The Hatrurim Basin in the Negev Desert, Israel, and Nahal Halamish – the locality of allabogdanite-bearing assemblages. (**c**) Eastward view on the Hatrurim Basin, Israel (hills beyond the road 258). Width of panorama is ca. 10 km. The base for Figure 1a,b was adapted from Britvin et al. (2015) (CC 4.0); the panorama was created by S.N.B.

Figure 2. The idealized relationship between the unit cells of barringerite and allabogdanite. The dashed lines define the allabogdanite cell. Projection onto {001}(barringerite) = {010}(allabogdanite). The *c*-axis of barringerite coincides with (and approximately equal to) the *b*-axis of allabogdanite and is perpendicular to the image plane. c(allabogdanite) ≈ $\frac{2}{3}a$(barringerite)$\sqrt{3}$.

Figure 3. General view of an allabogdanite-barringerite assemblage from the Hatrurim Basin. (**a**) Polished cross-section of diopside microbreccia containing allabogdanite and barringerite grains (white pebbles), photo in reflected light. (**b**) The same fragment; electron backscatter diffraction (EBSD) maps superimposed onto the SEM image of back-scattered electrons (BSE). Yellow grains denote barringerite (colored irrespective of crystallographic orientation), mottled ones are allabogdanite. Grain numbers correspond to those indicated in Table 1. The area corresponding to Figure 4 is marked by red square. Di – diopside.

Figure 4. Detailed view of barringerite-allabogdanite grain #3 (a red square on Figure 3). (**a**) Photo in reflected light. Mur - murashkoite (FeP) rims replacing allabogdanite and barringerite. (**b**) EBSD inverse pole figure (IPF) map of grains #3 and #5. Note that grain #3 is composed of a barringerite

Always consult and cite the final, published document. See http:/www.minsocam.org or GeoscienceWorld

This is the peer-reviewed, final accepted version for American Mineralogist, published by the Mineralogical Society of America.
The published version is subject to change. Cite as Authors (Year) Title. American Mineralogist, in press.
DOI: https://doi.org/10.2138/am-2021-7621. http://www.minsocam.org/

single crystal and allabogdanite trilling. Allabogdanite domains are shown by labels colored according to the scheme of trilling shown in (**c**). (**c**) Orientation of barringerite single crystal and three domains of cyclic allabogdanite twin (trilling) in grain #3 (see Table 3). Abg, allabogdanite; Brr, barringerite; Mur, murashkoite. Extended information on EBSD mapping of grains #3 and #5 are given in Supplementary Data (Figure S1).

Figure 5. Multiply twinned allabogdanite grain intergrown with pyrrhotite-4*C*. (**a**) SEM BSE image. The "X" letter marks the grain which was used for high-pressure high-temperature DAC experiments. (**b**) Photo in reflected light. (**c**) EBSD IPF orientation map. Black areas indicate unindexed points and unmapped regions. Abg, allabogdanite; Po, pyrrhotite.

Figure 6. Single crystals of allabogdanite in the Onello iron meteorite. Polished section after nital etching. SEM BSE image. Legend: Abg, allabogdanite; α-(Fe,Ni), kamacite; γ-(Fe,Ni), taenite.

Figure 7. X-ray diffraction patterns illustrating phase transition of allabogdanite to barringerite upon heating at atmospheric pressure. (**a**) Allabogdanite (grain #7 in Figure 3) heated under argon flow to 800°C. (**b**) The same grain heated to 850°C.

Figure 8. Phase transitions of allabogdanite from the Dead Sea upon compression and heating in the laser-heated diamond anvil cells (LHDAC). Fragments of a grain depicted on Figure 5a; chemical composition is given in Table 1. Data on the unit-cell parameters are presented in Table 5. Note the change of calculated density (D_{calc}, left scale) and unit-cell parameters (right scale) during phase transitions at 7.4 and 28.4 GPa, respectively. The errors (esd's) are smaller than the size of the symbols.

Always consult and cite the final, published document. See http:/www.minsocam.org or GeoscienceWorld

This is the peer-reviewed, final accepted version for American Mineralogist, published by the Mineralogical Society of America.
The published version is subject to change. Cite as Authors (Year) Title. American Mineralogist, in press.
DOI: https://doi.org/10.2138/am-2021-7621. http://www.minsocam.org/

519 The orientation relationships between unit-cell axes of allabogdanite and barringerite are shown in

520 Figure 2. Abg, allabogdanite; Brr, barringerite; RT, room temperature.

521

522

Always consult and cite the final, published document. See http:/www.minsocam.org or GeoscienceWorld

Table 1. Elemental composition of allabogdanite and barringerite from the Dead Sea basin.

Allabogdanite, wt.%						Allabogdanite, *apfu* (Σ = 3) [a]					Grain # [b]
Fe	Ni	Co	Mo	P	Total	Fe	Ni	Co	Mo	P	
76.23	1.74	0.33	0.47	21.36	100.13	1.95	0.04	0.008	0.007	0.99	#01
75.72	1.62	0.14	0.31	21.94	99.73	1.94	0.04	0.003	0.005	1.01	#03 [c]
76.24	1.95	0.18	0.41	21.35	100.13	1.95	0.05	0.004	0.006	0.99	#07
76.33	1.45	0.14	0.19	21.65	100.20 [d]	1.95	0.04	0.003	0.003	1.00	#12
76.66	1.44	0.16	0.29	21.59	100.14	1.96	0.04	0.004	0.004	1.00	#13
76.24	1.64	0.19	0.33	21.58	100.07	1.95	0.04	0.005	0.005	1.00	Avg. of 5
0.34	0.21	0.08	0.11	0.24							Std. dev.
71.88	4.13	0.15	2.47	21.40	100.03	1.86	0.10	0.004	0.037	1.00	Figure 5a [e]

Barringerite, wt.%						Barringerite, *apfu* (Σ = 3) [a]					
Fe	Ni	Co	Mo	P	Total	Fe	Ni	Co	Mo	P	Grain # [b]
76.04	1.79	0.33	0.34	21.14	99.64	1.96	0.04	0.008	0.005	0.98	#02
75.84	1.65	0.14	0.20	21.93	99.76	1.94	0.04	0.003	0.003	1.01	#03 [c]
76.18	1.95	0.31	0.32	21.67	100.43	1.94	0.05	0.007	0.005	1.00	#04
75.73	1.81	0.15	0.23	21.64	99.56	1.95	0.04	0.004	0.003	1.00	#05
75.52	2.08	0.12	0.38	21.59	99.69	1.94	0.05	0.003	0.006	1.00	#06
76.07	1.79	0.16	0.68	21.47	100.17	1.95	0.04	0.004	0.010	0.99	#08
77.08	2.07	0.13	0.28	21.20	100.76	1.97	0.05	0.003	0.004	0.98	#10
76.45	1.76	0.20	0.31	21.29	100.01	1.96	0.04	0.005	0.005	0.99	#11
76.41	1.52	0.14	0.43	21.67	100.59 [f]	1.95	0.04	0.003	0.006	1.00	#14
75.86	1.68	0.17	0.18	21.45	99.34	1.96	0.04	0.004	0.003	1.00	#15
76.12	1.81	0.19	0.34	21.51	99.97	1.95	0.04	0.005	0.005	1.00	Avg. of 10
0.45	0.18	0.07	0.14	0.24							Std. dev.
56.19	22.36	0.18	0.25	21.16	100.14	1.45	0.55	0.004	0.004	0.99	#09, max Ni
73.36	5.34	0.18	0.29	21.32	100.49	1.88	0.13	0.004	0.004	0.98	#09, min Ni

[a] *apfu* = atoms per formula unit. [b] Grain numbers correspond to those indicated in Figure 3. [c] Intergrowth of allabogdanite and barringerite (Figure 4). [d] Contains vanadium, 0.44 wt.% (0.01 atoms per formula unit). [e] The grain used in high-pressure high-temperature experiments. [f]Contains vanadium, 0.42 wt.% (0.01 atoms per formula unit).

Table 2. Crystallographic data for allabogdanite and barringerite grains #1 and #5

	Allabogdanite #1	Barringerite #5
Crystal system	Orthorhombic	Hexagonal
Space group	*Pnma*	$P\bar{6}2m$
a (Å)	5.832 (2)	5.8618 (13)
b (Å)	3.5971 (13)	
c (Å)	6.713 (2)	3.4598 (11)
V (Å^3)	140.83 (9)	102.95 (6)
Z	4	3
V/*Z* (Å^3)	35.20	34.32
D_{calc} (g cm^{-3})	6.729	6.903

Table 3. Euler orientation matrices of allabogdanite domains in grain #03 (Figure 4) [a]

Domain #	Mass fraction (%)	Isolated / overlapped reflections	Orientation matrix
1	41	4560 / 1596	[1 0 0] [0 1 0] [0 0 1]
2	32	4560 / 1592	[–½ 0 –¾] [0 1 0] [1 0 –½]
3	27	4553 / 1599	[½ 0 –¾] [0 1 0] [1 0 ½]

[a] Domain #2 is rotated by –120°; domain #3 by 60° around [010]. See datablock Allabogdanite_Trilling_hklf5 in the attached CIF file. Software used: CrysAlisPro (2018).

Table 4. Rotation matrices of allabogdanite and barringerite domains before and after thermally induced allabogdanite→barringerite transition (grain #13)

Domain #	Mass fraction (%)	Rotation angle (°)	Rotation axis		
			h	*k*	*l*
Allabogdanite before transition					
1	39	0	0	1	0
2	23	120.02	0	1	0
3	24	59.70	0	1	0
Barringerite after transition					
1	48	0	1	0	0
2	40	–146.49	0.61	–0.06	–0.79
3	2	90.11	0	–0.13	–0.99

560

561 **Table 5.** *In situ* phase transitions of allabogdanite upon compression/heating in diamond anvil cells [a]
562

Run [b]	*P* (GPa)	*T* (°C) [c]	Phase [d]	*a* (Å)	*b* (Å)	*c* (Å)	*V*/*Z* (Å^3)	D_{calc} (g cm^{-1})
0	0.0	–	Abg	5.7800(1)	3.5637(1)	6.6478(3)	34.23	7.008
1	2.0	–	Abg	5.7429(13)	3.5581(15)	6.6245(11)	33.84	7.089
1	4.8	–	Abg	5.6953(5)	3.5484(6)	6.5973(4)	33.33	7.197
2	*7.4*	*–*	*Abg*	*5.6487(9)*	*3.5424(14)*	*6.571(18)*	*32.87*	*7.298*
2	*7.4*	*1350*	*Brr*	*5.7747(4)*		*3.4439(2)*	*33.15*	*7.236*
2	13.5	1350	Brr	5.7360(8)		3.3787(4)	32.09	7.476
1	19.6	1350	Brr	5.677(15)		3.3694(8)	31.34	7.654
2	22.0	1350	Brr	5.6356(4)		3.3682(2)	30.88	7.769
2	*28.4*	*–*	*Brr*	*5.5954(5)*		*3.3368(3)*	*30.16*	*7.955*
2	*28.4*	*1400*	*Abg*	*5.423(7)*	*3.4558(8)*	*6.3853(9)*	*29.92*	*8.019*
2	32.2	1400	Abg	5.346(2)	3.4474(3)	6.3958(3)	29.47	8.142
2	39.0	1400	Abg	5.307(3)	3.4356(4)	6.3701(5)	29.04	8.262

563
564 [a] Single-crystal fragments of a grain marked as "X" in Figure 5a (last analysis record in Table 1). Records
565 related to phase transition points are typed in italic. [b] Run #0 – measurement under ambient conditions; runs #2
566 and #3 – compression/heating experiments. [c] Accuracy of temperature measurements: ±100 °C. [d] Abg,
567 allabogdanite; Brr, barringerite.
568

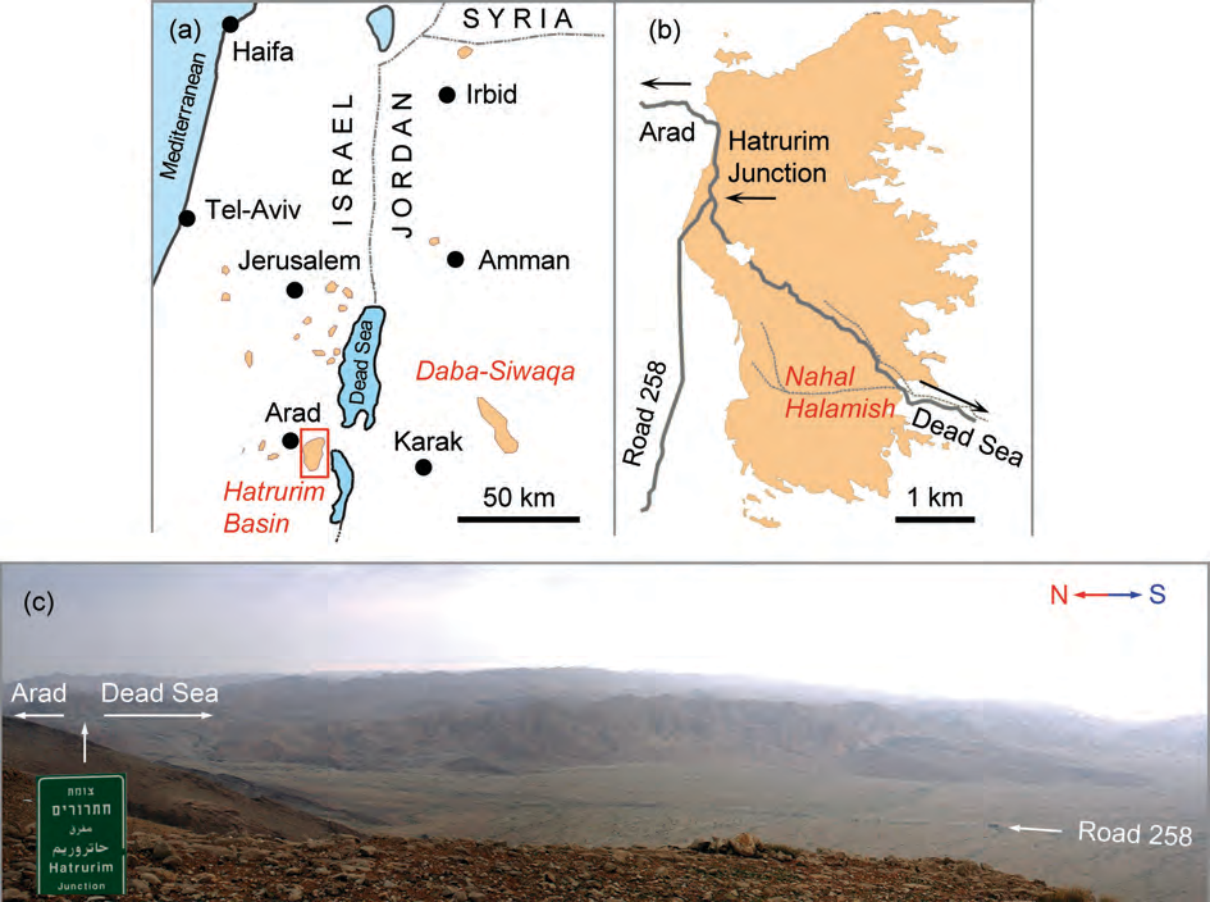
(a)
Haifa
Mediterranean
SYRIA
Irbid
ISRAEL
JORDAN
Tel-Aviv
Jerusalem
Amman
Dead Sea
Daba-Siwaqa
Arad
Karak
Hatrurim
Basin
50 km
(b)
Arad
Hatrurim
Junction
Road 258
Nahal
Halamish
Dead Sea
1 km
(c)
N
S
Arad
Dead Sea
Hatrurim
Junction
Road 258

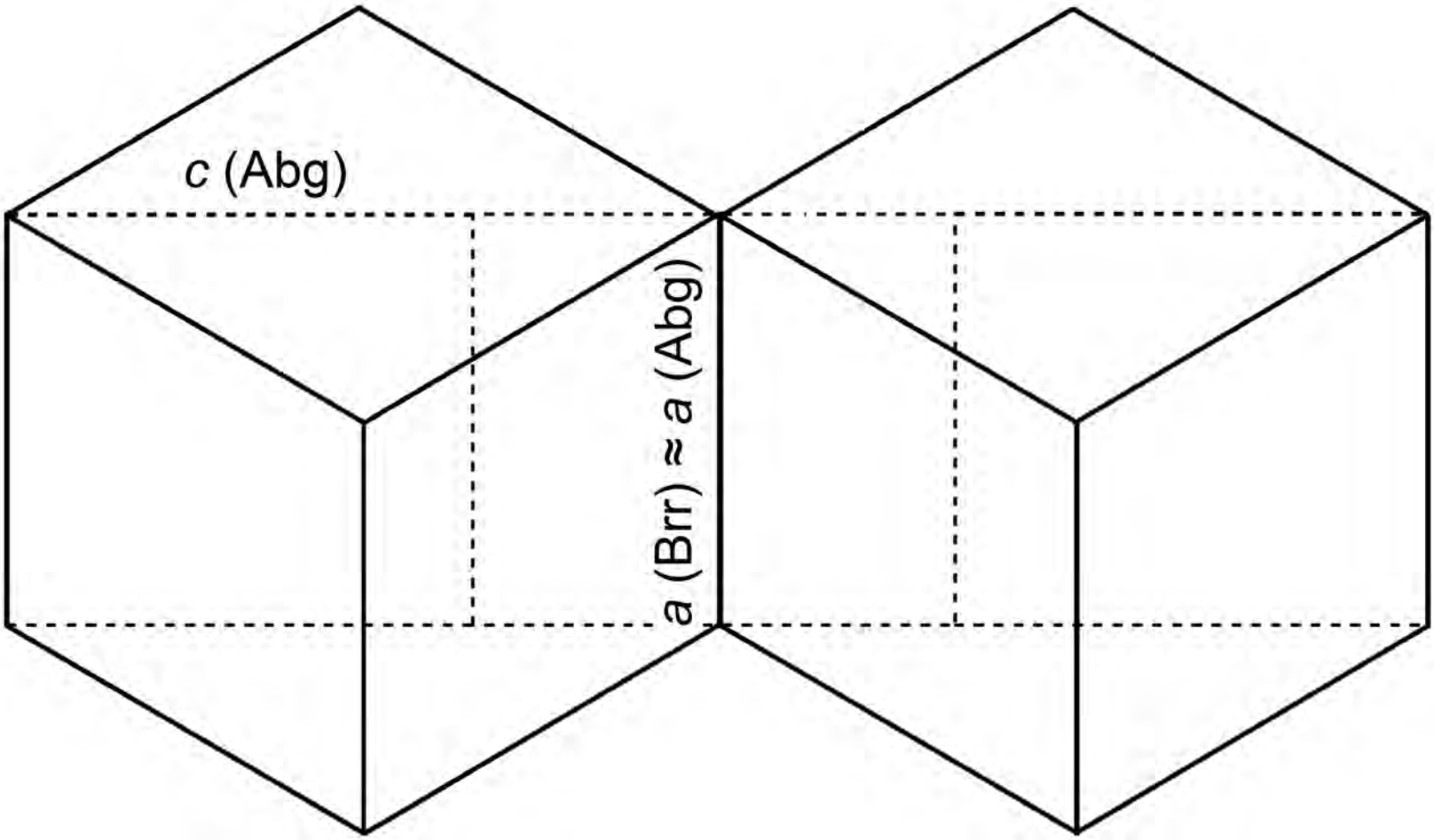
c (Abg)
a (Brr) ≈ a (Abg)

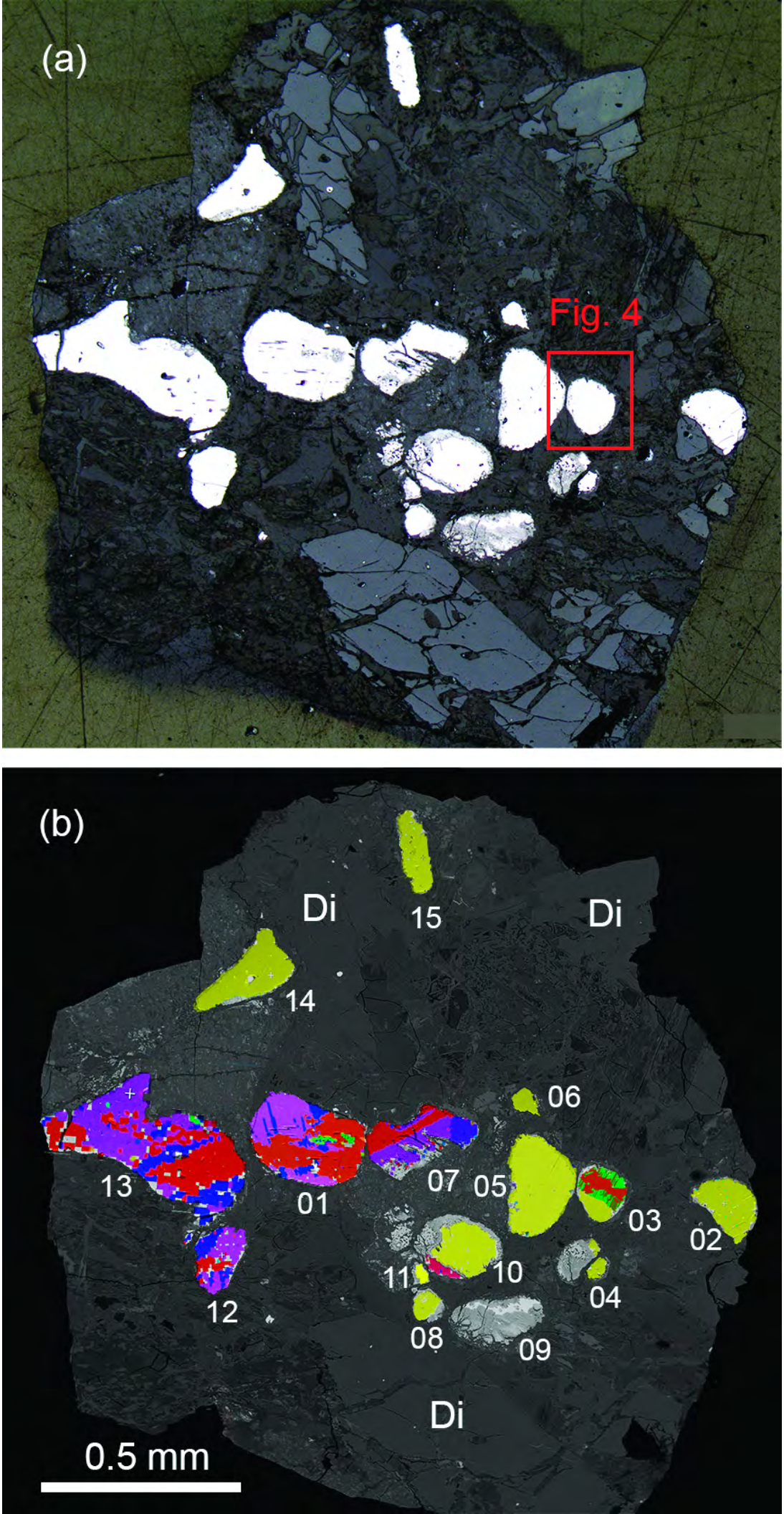
(a)
Fig. 4
(b)
Di
15
Di
14
06
13
07
05
01
03
02
11
10
04
12
08
09
Di
0.5 mm

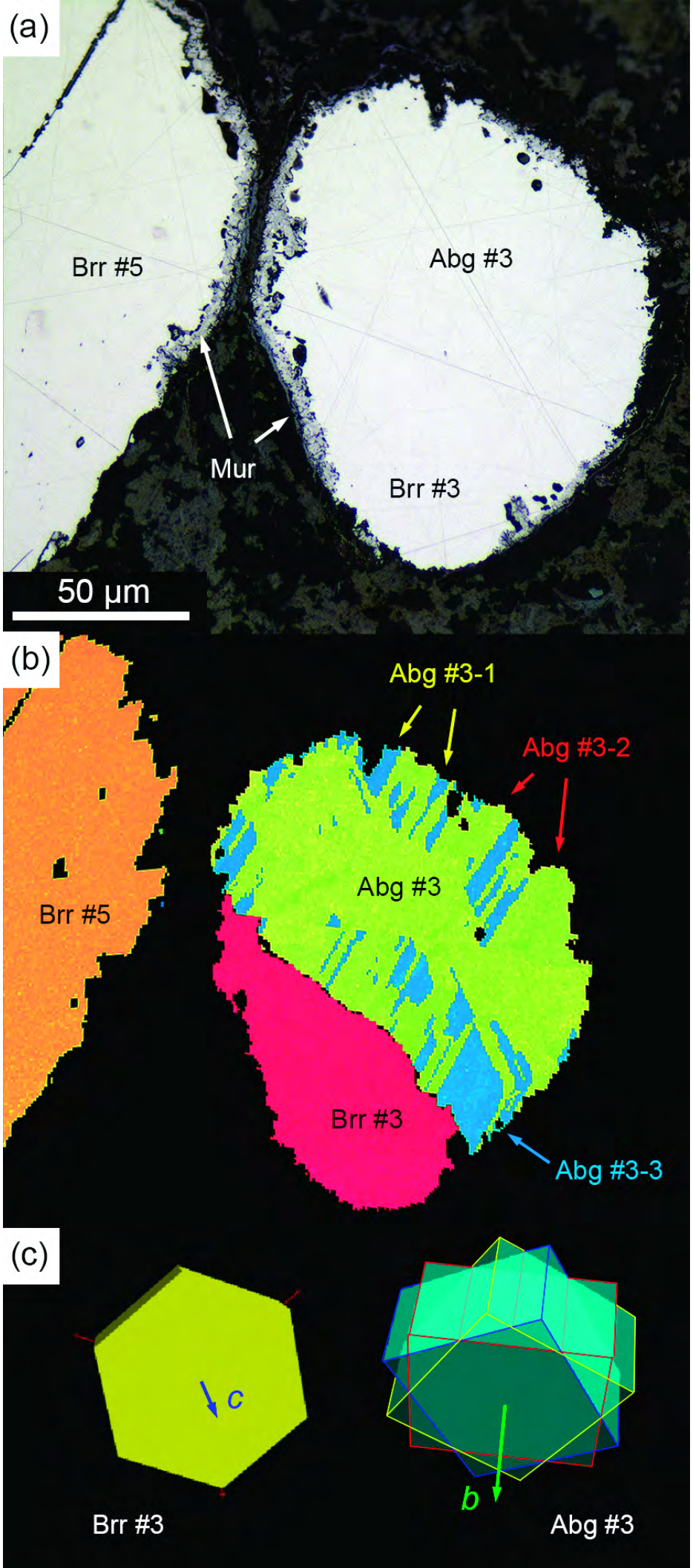
(a)
Brr #5
Abg #3
Mur
Brr #3
50 μm
(b)
Abg #3-1
Abg #3-2
Brr #5
Abg #3
Brr #3
Abg #3-3
(c)
c
b
Brr #3
Abg #3

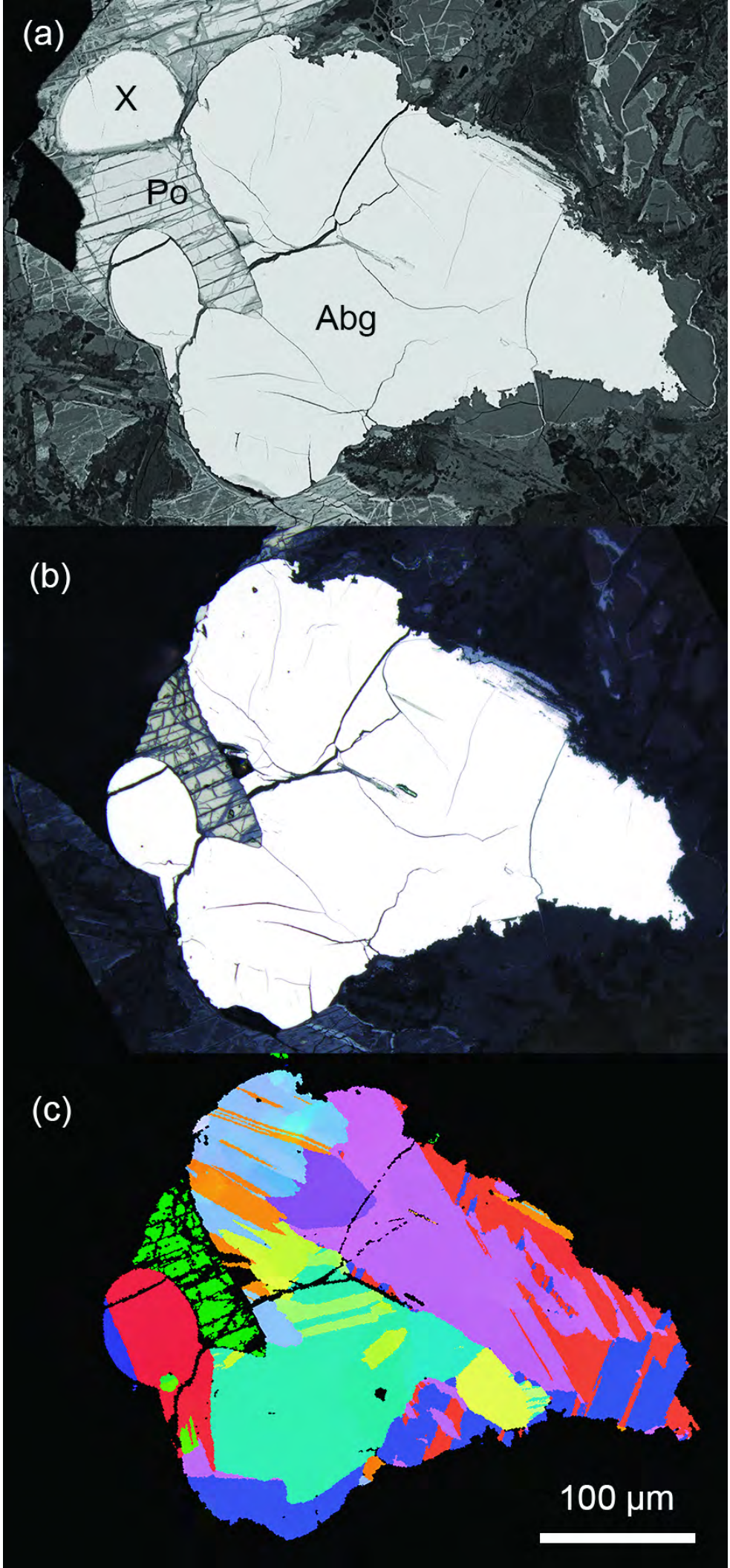
(a)
X
Po
Abg
(b)
(c)
100 µm

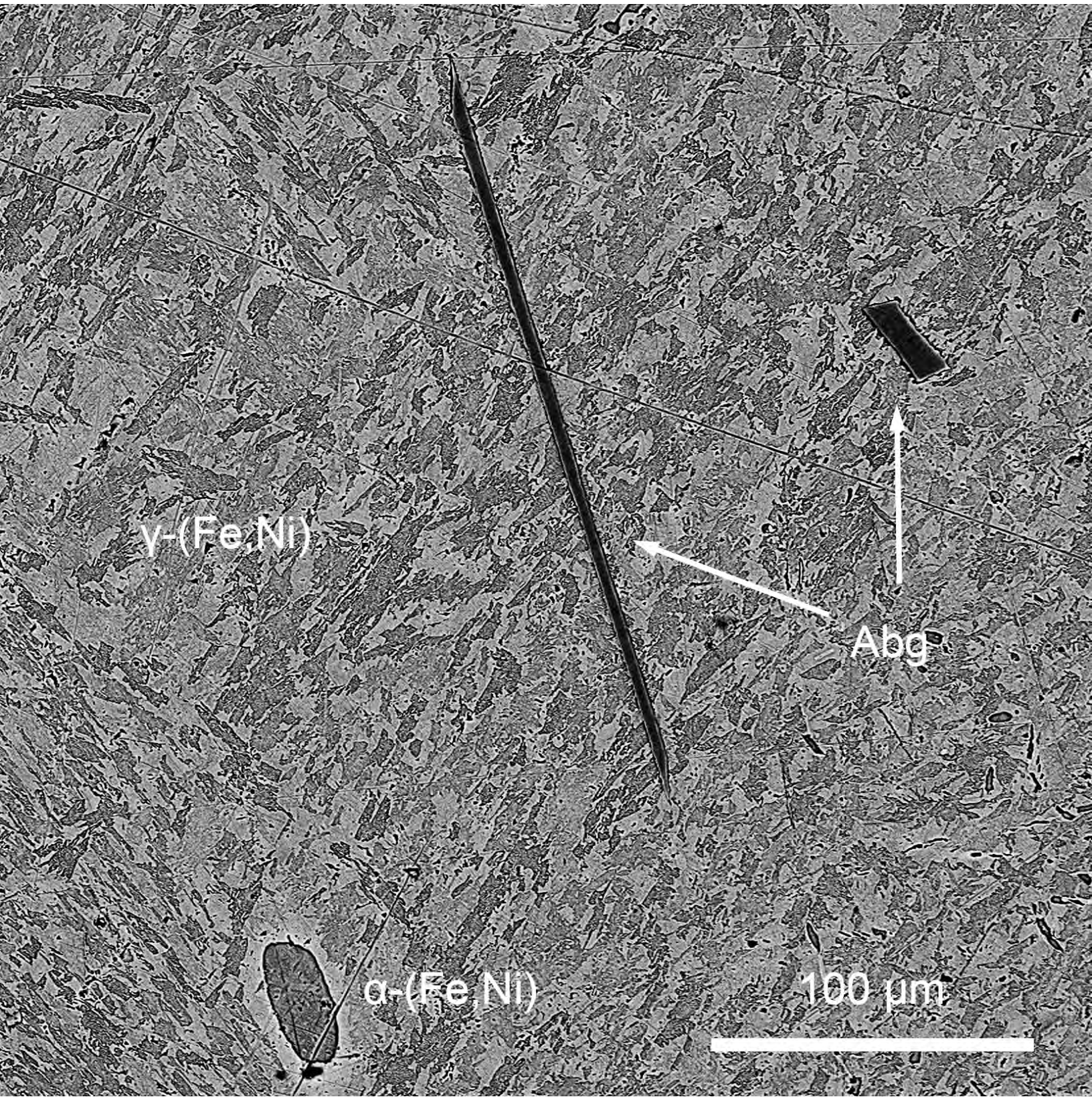
γ-(Fe,Ni)
Abg
α-(Fe,Ni)
100 µm

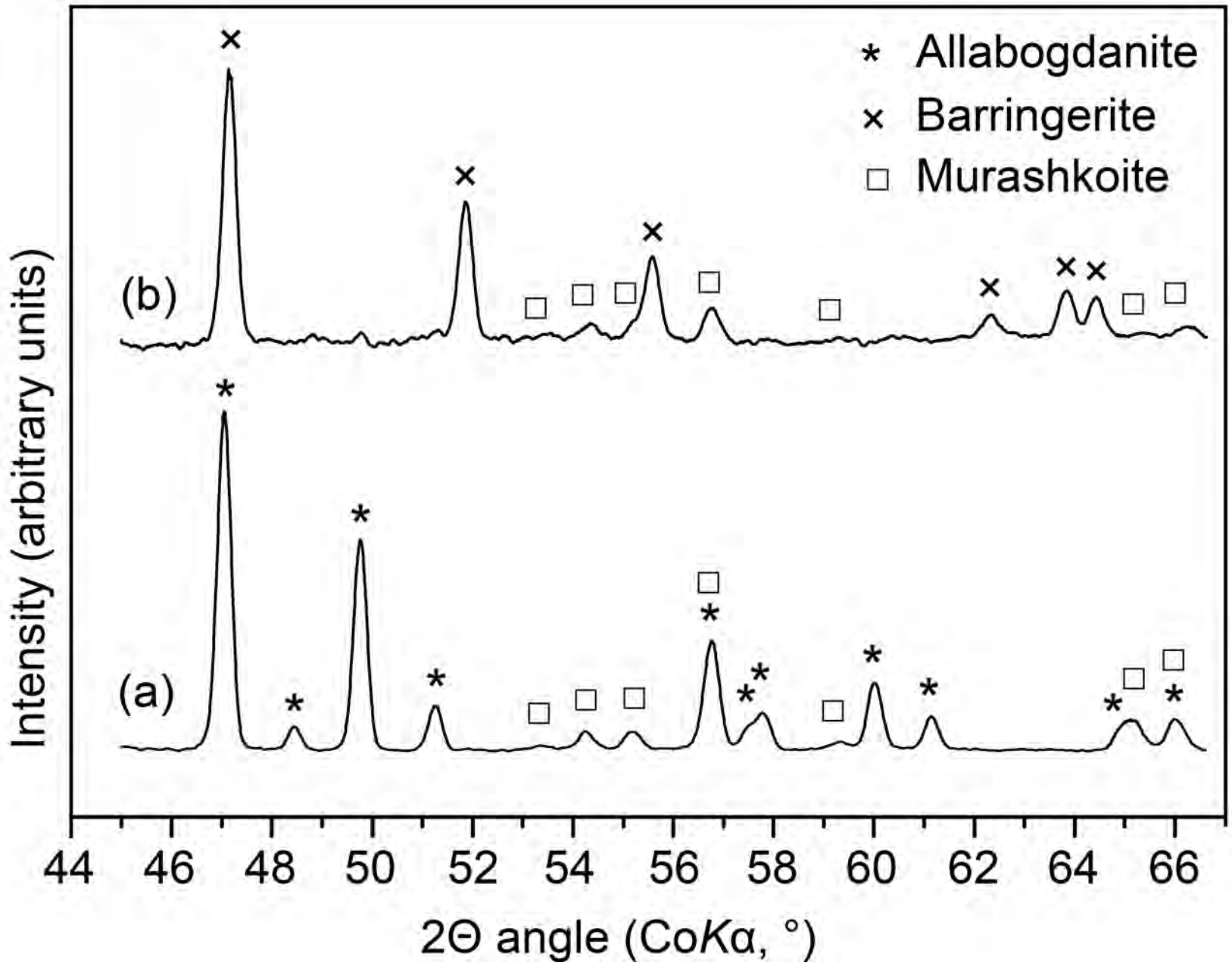
* Allabogdanite
× Barringerite
□ Murashkoite
(b)
(a)
Intensity (arbitrary units)
44
46
48
50
52
54
56
58
60
62
64
66
2Θ angle (CoKα, °)

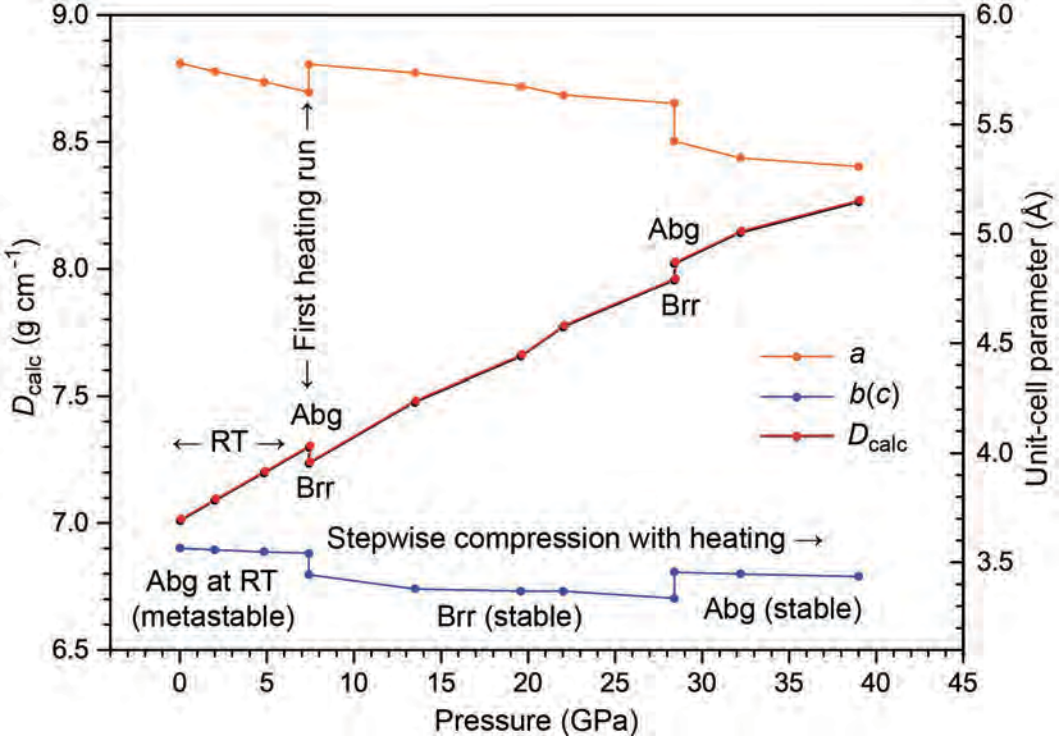
9.0
8.5
8.0
7.5
7.0
6.5
D_{calc} (g cm^{-1})
6.0
5.5
5.0
4.5
4.0
3.5
Unit-cell parameter (Å)
0
5
10
15
20
25
30
35
40
45
Pressure (GPa)
First heating run →
← RT →
Abg
Brr
Abg
Brr
a
b(c)
D_{calc}
Stepwise compression with heating →
Abg at RT
(metastable)
Brr (stable)
Abg (stable)